



Oxygen reduction on Pd_3Pt_1 bimetallic nanoparticles highly loaded on different carbon supports

Wei He^a, Mei Chen^b, Zhiqing Zou^b, Zhilin Li^b, Xiaogang Zhang^a, Seon-Ah Jin^c, Dae Jong You^c, Chanho Pak^c, Hui Yang^{b,*}

^a College of Materials Science and Engineering, Nanjing University of Aeronautics and Astronautics, Nanjing 210016, China

^b Shanghai Institute of Microsystem and Information Technology, Chinese Academy of Sciences, 865 Changning Road, Shanghai 200050, China

^c Energy Lab., Emerging Technology Center, Samsung Advanced Institute of Technology (SAIT), Samsung Electronics, Suwon 440-600, Republic of Korea

ARTICLE INFO

Article history:

Received 8 January 2010

Received in revised form 28 March 2010

Accepted 13 April 2010

Available online 18 April 2010

Keywords:

Pd–Pt alloy

Carbon nanotube

Ordered mesoporous carbon

Electrocatalysis

Oxygen reduction reaction

Methanol tolerance

ABSTRACT

The development of new cost-effective cathode catalysts with high methanol tolerance and at a high catalyst loading is highly desirable for the direct methanol fuel cell. The Pd_3Pt_1 bimetallic alloy nanoparticles highly loaded on different carbon supports, including Vulcan XC-72R carbon, single and multi-walled carbon nanotubes (SWCNTs/MWCNTs) and ordered mesoporous carbon (OMC), have been prepared by a modified polyol reduction route. The activities of the catalysts for the oxygen reduction reaction (ORR) have been studied based on the rotating disk and ring-disk electrode (RDE/RRDE) techniques in pure and methanol-containing electrolytes. X-ray diffraction indicates that all the Pd_3Pt_1/C nanoparticles evidence a single-phase fcc disordered structure. The mean particle size of Pd_3Pt_1 alloy nanoparticles on different supports is ca. 4–5 nm even at a metal loading of 50 wt%. Among various carbons supported catalysts, the highest ORR activity, found on the OMC-supported Pd_3Pt_1 catalyst, even surpasses that on the commercial Pt/C catalyst. Kinetic analysis reveals that the ORR on the Pd_3Pt_1/OMC catalyst predominantly undergoes a four-electron process, leading to water formation. Furthermore, the Pd_3Pt_1/OMC catalyst exhibited a higher methanol tolerance during the ORR than the commercial Pt/C catalyst; ensuring a higher ORR performance while diminishing Pt utilization.

© 2010 Elsevier B.V. All rights reserved.

1. Introduction

Because of system simplicity and environmental friendliness, the direct methanol fuel cell (DMFC) has been considered as a promising energy converter for a variety of portable applications [1,2]. However, several challenges need to be addressed before its practical application. Examples include the high costs of Pt-based catalysts, slow kinetics of both anode and cathode reactions and the crossover of methanol from the anode to the cathode. In particular, the activity improvement of the oxygen reduction reaction (ORR) represents one of the important issues in fuel cell development. To address the crossover problem, one strategy is the development of novel ORR catalysts with high catalytic activity and good methanol tolerance [3,4]. Efforts to this end have involved the utilization of Pd-based alloy catalysts, not only because of the lower costs and more abundance but also because of the lower reactivity observed for the Pd-based alloys toward methanol oxidation [5,6]. The ORR activity enhancement on these Pd alloy catalysts

has been attributed to several factors, including effects that are electronic and structural in nature [7–9]. Among the Pd–M alloy catalysts investigated in the literature, novel Pd–Pt alloy catalyst might be a promising candidate as methanol-tolerant ORR catalysts [10–12] because the long-term stability of Pd in acidic solution is comparable with Pt.

It is well known that the basic properties of supported catalysts are strongly influenced by the impregnation method, the microscopic nature of the structure, the surface reactivity, the metal precursor used, and the dispersion of nanoparticles. For the latter issue, the morphology and nanostructure of carbon supports are considered to be main factors in obtaining high dispersion and thus enhanced catalytic activities of nanoparticle catalysts [13,14]. Efforts to this issue have involved the exploration of various carbon materials as supports, such as activated carbon, single and multi-walled carbon nanotubes (SWCNTs/MWCNTs) [15,16], carbon nanofibers [17] and ordered mesoporous carbons (OMCs) [18]. Especially, the OMCs, due to their appealing structural characteristics such as periodic and uniform mesopores and high surface area, have recently received much attention for their potential use as catalyst supports in fuel cells. Nanoporous carbons with 3D ordered pore structures have also demonstrated to improve the

* Corresponding author. Fax: +86 21 32200534.

E-mail addresses: huiyang65@hotmail.com, hyang@mail.sim.ac.cn (H. Yang).

mass transport of reactants and by-products during fuel cell operation [19–21]. For example, Ryoo and co-workers [22] described a general strategy for the synthesis of highly ordered, rigid arrays of nanoporous carbon having uniform but tunable diameters (typically 6 nm inside and 9 nm outside). The resulting material supports a high dispersion of platinum nanoparticles. The high dispersion of these platinum clusters gives rise to promising electrocatalytic activity for the ORR. Vengatesan et al. [23] synthesized mesoporous carbons using soft colloidal template route, and supported Pt catalysts by aqueous impregnation. With such an OMC material, a better dispersion and higher Pt utilization was obtained as compared with that of the Pt/C catalyst at the same loading, originated respectively from a higher surface area and the highly ordered mesopore structure. Clearly, the effect of the substrate seems to be responsible for the enhancement in electrocatalytic activity as well as the improvement in fuel cell performance. Also, fuel cell catalysts should be at a high metal loading level and on an adequate support in order to reduce the inner electrical resistance of the catalytic layer [24] and to enhance the rate of proton diffusion and reactant permeability within the catalytic layer.

In this work, research emphasis is placed on the effect of various carbon supports on the ORR activity on the Pd_3Pt_1 bimetallic nanoparticles at a high metal loading [25]. ORR activities on the catalysts with different carbon supports were evaluated in the absence and presence of methanol. Also, ORR pathway on the catalysts was analyzed using a rotating disk electrode (RDE) and a rotating ring-disk electrode (RRDE) technique.

2. Experimental

2.1. Catalysts synthesis

Carbon-supported Pd–Pt alloy catalyst was prepared by a modified ethylene glycol (EG) reduction route; herein trisodium citrate (TC) was used as a complexing agent and stabilizer; and the carbon supports used are Vulcan XC-72R, SWCNTs, MWCNTs and OMC. Purified SWCNTs and MWCNTs are commercial products from Shenzhen Nanotech. Port. Co. Ltd. without further functionalization. The OMC support was obtained from SAIT with a surface area of $680\text{ m}^2\text{ g}^{-1}$ and a pore size of 5 nm [26,27]. Topically, a given amount of carbon material, TC, palladium acetylacetone $[\text{Pd}(\text{acac})_2]$ and platinum acetylacetone $[\text{Pt}(\text{acac})_2]$ were dispersed in 50 mL of EG to form a mixture in a three-necked flask. The flask was sealed and then insufflated pure N_2 to replace the air. Subsequently, such a mixture was maintained at a refluxing temperature of 175°C for 6 h. After cooling to room temperature, the mixture was filtrated, washed copiously with water and dried under vacuum at 75°C for 12 h. The total metal loading was controlled at 50 wt% for all the catalysts. The as-prepared Pd–Pt alloy catalysts are labeled as $\text{Pd}_3\text{Pt}_1/\text{XC-72R}$, $\text{Pd}_3\text{Pt}_1/\text{SWCNTs}$, $\text{Pd}_3\text{Pt}_1/\text{MWCNTs}$, and $\text{Pd}_3\text{Pt}_1/\text{OMC}$, respectively.

2.2. Physical characterization

X-ray diffraction (XRD) measurements were conducted using a Rigaku D/MAX-2000 diffractometer with Cu K_α radiation. The tube voltage and current were maintained at 40 kV and 100 mA, respectively. Diffraction patterns were collected with a scanning rate of 2° min^{-1} and with a step of 0.02° . The sample for transmission electron microscopy (TEM) analysis was prepared by ultrasonically suspending catalyst powder in ethanol. A drop of suspension was then placed onto a holey copper grid and dried under air. The morphology of the catalysts was characterized using a JEOL JEM 2100F operated at 200 kV.

2.3. Electrochemical characterizations

Porous electrodes were prepared as follows: 10 mg of Pd–Pt alloy catalyst, 0.5 mL of Nafion (5 wt%, Aldrich) and 2.5 mL of ultrapure water were mixed ultrasonically. Then, 3 μL of this ink was transferred onto a glassy carbon disk (GC, 3 mm in diameter), and left to dry overnight. Each electrode contained ca. $70.7\text{ }\mu\text{g cm}^{-2}$ of the metal. Electrochemical measurements were performed using a CHI 730 Potentiostat and a conventional three-electrode cell. The catalytic activity for the ORR was measured with a rotating disk electrode and a rotating ring-disk electrode mounted with a BM-ED 1101 electrode (Radiometer, France). The counter electrode was a GC plate, and a saturated calomel electrode was used as the reference electrode. All potentials, however, are referenced with respect to the reversible hydrogen electrode (RHE). The real surface areas of all the catalysts were determined by hydrogen desorption and CO_{ad} oxidation in CO stripping voltammetry. The oxidation charges of monolayer adsorption of CO and hydrogen on Pt or Pd surface are assumed to be 420 and $210\text{ }\mu\text{C cm}^{-2}$, respectively [8,28]. High-purity nitrogen or oxygen was used for deaeration of the solutions. During the measurements, a gentle gas flow was kept above the electrolyte.

For DMFC test, the membrane electrode assembly (MEA) was made by sandwiching a pre-treated Nafion 117 membrane between the anode and cathode by hot-pressing at 130°C at 6 MPa for 3 min [29]. In the case of anode, slurry consisting of MWNTs and PTFE (weight ratio 4:1) was coated on carbon paper (TGP-H-060, 0 wt% PTFE, Toray) to serve as anodic micro-porous layer (MPL), in which 1D MWNTs as anode MPL is beneficial to the methanol mass transfer [29]. On top of this layer, the catalyst was then sprayed in the form of a homogenous ink, which was prepared by ultrasonication the required amount of Pt–Ru (1:1) black, Pt–Ru/C (Pt loading: 40%; Ru loading: 20%), and 5 wt% Nafion (DuPont) solution into a mixture of isopropyl alcohol and ultrapure water with a volume ratio of 1:1. For cathode, a suspension of Vulcan XC-72R and PTFE (weight ratio 4:1) was scraped onto carbon paper (TGP-H-060, 20 wt% PTFE, Toray) as MPL. Subsequently, an ink containing 25 wt% Nafion and catalyst was pasted on it. The cathode catalysts were the as-prepared $\text{Pd}_3\text{Pt}_1/\text{OMC}$ and commercial 60 wt% Pt/C(JM-9000), respectively. The metal loading is 4.0 mg cm^{-2} for both anode and cathode, and the active area of the MEA is 4.0 cm^2 . The polarization curves of MEAs were obtained on Arbin FCT system (Arbin Inc., USA). For each discharging current point along the polarization curve, a period of 2 min waiting time was used to obtain the stable voltage. 3 and 5 M aqueous methanol solution were injected into anode reservoir and the cathode was operated under air-breathing mode.

All the electrochemical measurements were performed in a thermostated container at a temperature of ca. $25 \pm 1^\circ\text{C}$.

3. Results and discussion

3.1. XRD and TEM characterization

The average bulk composition of the Pd–Pt bimetallic catalysts was evaluated using an ICP-AES analysis. The obtained results are nearly the same as original stoichiometric values, suggesting that as a result of our synthesis methodology Pd and Pt are totally reduced to form Pd/Pt bimetallic nanoparticles.

Fig. 1 shows the XRD patterns of Pd_3Pt_1 nanoparticles on different carbon supports and the commercial Pt/C(JM-9000) catalyst with Pt loading of 60 wt%. All the XRD patterns clearly show five main characteristic peaks of face-centered-cubic (fcc) crystalline Pd, namely, the planes $(1\ 1\ 1)$, $(2\ 0\ 0)$, $(2\ 2\ 0)$, $(3\ 1\ 1)$ and $(2\ 2\ 2)$, demonstrating that all the catalysts mainly possess a single phase

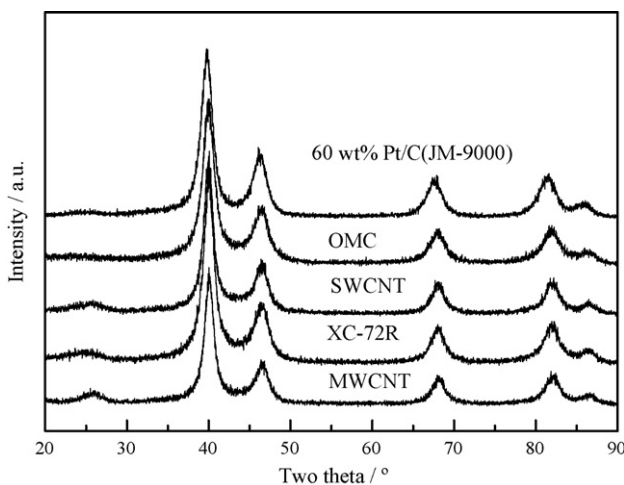


Fig. 1. XRD patterns of the Pd–Pt alloy catalysts and commercial Pt/C(JM-9000) catalysts.

fcc disorder structure (i.e., solid solutions). Relative to the same reflections in Pd/C or Pt/C, the diffraction peaks for the Pd–Pt catalysts are shifted slightly to lower or higher 2θ values, indicative of formation of an alloy involving the incorporation of Pt in the fcc structure of Pd. For as-prepared Pd–Pt catalysts with the Pd/Pt atomic ratio of 3:1, the obtained lattice constant is ca. 3.899 Å, which almost lies on the straight line between the theoretical lattice constant (Pt: 3.9231 Å and Pd: 3.8902 Å) for Pt–Pd particles and Pd content [30,31], indicating that lattice constant for our $\text{Pd}_3\text{Pt}_1/\text{C}$ samples follows Vegard's law for Pd–Pt solid solution and well-alloyed catalysts were obtained. The average crystalline sizes of these catalysts are calculated based on the X-ray linewidths of (2 2 0) reflection using the Scherrer equation. The obtained mean particle sizes for different catalysts are in the range of 4–5 nm even at a high metal loading, as provided in Table 1. It can be seen that the particle size of the $\text{Pd}_3\text{Pt}_1/\text{OMC}$ catalyst is the smallest among the catalysts, which may be ascribed to the high surface area of OMC ($>600 \text{ m}^2 \text{ g}^{-1}$) and to its ordered mesopores.

TEM micrographs of the as-prepared catalysts provide more details on the particle shape and size distribution of the catalysts. Fig. 2 shows three typical TEM images of the $\text{Pd}_3\text{Pt}_1/\text{XC-72R}$, $\text{Pd}_3\text{Pt}_1/\text{SWCNTs}$ and $\text{Pd}_3\text{Pt}_1/\text{OMC}$ catalyst. As observed, Pd–Pt alloy particles were well distributed onto the surface of XC-72R (Fig. 2a) and SWCNTs bundles (Fig. 2b) with the mean particle diameters of 4.4 and 5.0 nm, respectively. These values are in fairly good agreement with the XRD results. The TEM image in Fig. 2c shows that small Pd–Pt nanoparticles of ca. 4.1 nm are supported on the surface of the OMC particles. However, TEM images provided by one of the authors [27] for 60 wt% Pt loaded OMC in 3D revealed that Pt particles are 3D spatially distributed in a uniform and homogenous manner within the OMC particles. Thus, in the case of the $\text{Pd}_3\text{Pt}_1/\text{OMC}$ catalyst, it is presumed that Pd–Pt alloy particles are supported both outside and inside the mesopores of the OMC; thus resulting in a highly dispersed state of the metal particles.

3.2. Electrochemical characterizations

The electrochemical properties of Pd–Pt alloy catalysts deposited on various carbon supports were first examined by cyclic voltammograms, as shown in Fig. 3. The stable profiles were obtained after 15 cycles. There are three distinct potential regions in the voltammograms: the hydrogen adsorption/desorption region between 0.05 and 0.31 V, the double-layer region between 0.31 and 0.60 V, and the surface oxide formation/reduction region ($>0.60 \text{ V}$) [32]. The change in double-layer region associated with the accessible surface area of carbon is in the order: $\text{Pd}_3\text{Pt}_1/\text{OMC} > \text{Pd}_3\text{Pt}_1/\text{XC-72R} > \text{Pd}_3\text{Pt}_1/\text{SWCNTs} > \text{Pd}_3\text{Pt}_1/\text{MWCNTs}$, which was in the same trend with particle size of Pd–Pt alloy catalysts on different carbon supports. For OMC-supported catalyst with the smallest metal particle size, its double-layer region is much larger than that for other carbon-supported catalysts, probably due to the higher surface area of the OMC. Both H region area and CO_{ad} oxidation area were used to calculate the electrochemically active surface area (ECSA) listed in Table 1. As can be seen, the ECSA_{CO} is larger than ECSA_{H} . But both of them are in the same trend and nearly proportional to the particle size.

Fig. 4 presents the ORR polarization curves for Pd–Pt catalysts with different carbon supports in oxygen-saturated 0.1 M HClO_4 at room temperature. From the figure, the ORR on all the catalysts is diffusion-controlled when the potential is less than 0.7 V and is under mixed diffusion kinetics control in the potential region between 0.7 and 0.85 V. For the sake of clarity, a close-up of this region was shown in the inset of Fig. 4. Among a variety of carbon materials, the ordered mesoporous carbon-supported Pd–Pt nanoparticles catalyst shows the highest ORR activity, and the ORR activity decrease in the order: $\text{Pd}_3\text{Pt}_1/\text{OMC} > \text{Pd}_3\text{Pt}_1/\text{SWCNTs} > \text{Pd}_3\text{Pt}_1/\text{XC-72R} > \text{Pd}_3\text{Pt}_1/\text{MWCNTs}$. At a given potential of 0.85 V, for the $\text{Pd}_3\text{Pt}_1/\text{MWCNTs}$, $\text{Pd}_3\text{Pt}_1/\text{XC-72R}$, $\text{Pd}_3\text{Pt}_1/\text{SWCNTs}$, Pt/C and $\text{Pd}_3\text{Pt}_1/\text{OMC}$ catalyst, the mass activities (MA) are 6.28, 8.64, 9.29, 10.44 and 14.02 mA mg^{-1} , and the specific activities (SA), a measure of the "intrinsic" kinetic performance of metal catalyst, are 27.28, 26.92, 35.40, 45.59 and $34.58 \text{ } \mu\text{A cm}^{-2}$, respectively; clearly assessing that the property of carbon support plays a significant role in the improvement of ORR activity.

As mentioned above, the ORR activity on $\text{Pd}_3\text{Pt}_1/\text{MWCNTs}$ is worse than that on $\text{Pd}_3\text{Pt}_1/\text{XC-72R}$. The poor dispersion of MWCNTs in EG as well as the high loading of catalyst result in the aggregated metal with a large particle size as shown in Table 1, which may lead to the inferior ORR activity of MWCNTs-supported Pd–Pt catalyst. Conversely, the $\text{Pd}_3\text{Pt}_1/\text{SWCNTs}$ catalyst exhibits a superior ORR activity to the $\text{Pd}_3\text{Pt}_1/\text{XC-72R}$, in spite of a similar particle size with the $\text{Pd}_3\text{Pt}_1/\text{MWCNTs}$, probably due to high electrochemically accessible area and high graphitic crystallinity of the SWCNTs [33,34]. In addition, the limiting current density of the ORR on $\text{Pd}_3\text{Pt}_1/\text{SWCNTs}$ is higher than that on the other catalysts. The thinner film electrode of the $\text{Pd}_3\text{Pt}_1/\text{SWCNTs}$ may be considered to lower the internal diffusion limitation of O_2 [35]. It may be also related to the transport properties of O_2 within different diffusion electrodes and/or the accessibility of different catalytic electrodes. However, the detailed reason is not well understood. Notably, the OMC-supported Pd–Pt

Table 1
XRD and electrochemical characterizations of the Pd–Pt alloy catalysts and commercial Pt/C(JM-9000).

Sample	Size/nm	$S_{\text{XRD}}/\text{m}^2 \text{ g}^{-1}$	$\text{ECSA}_{\text{H}}/\text{m}^2 \text{ g}^{-1}$	$\text{ECSA}_{\text{CO}}/\text{m}^2 \text{ g}^{-1}$	MA at 0.85 V/ mA mg^{-1}	SA _{CO} at 0.85 V/ $\mu\text{A cm}^{-2}$
$\text{Pd}_3\text{Pt}_1/\text{MWCNTs}$	5.0	83.55	19.42	23.02	6.28	27.28
$\text{Pd}_3\text{Pt}_1/\text{XC-72R}$	4.2	99.46	26.18	32.09	8.64	26.92
$\text{Pd}_3\text{Pt}_1/\text{SWCNTs}$	4.9	85.26	16.06	26.24	9.29	35.40
$\text{Pd}_3\text{Pt}_1/\text{OMC}$	4.0	104.44	29.01	40.54	14.02	34.58
Pt/C(JM-9000)	4.5	92.83	18.46	22.90	10.44	45.59

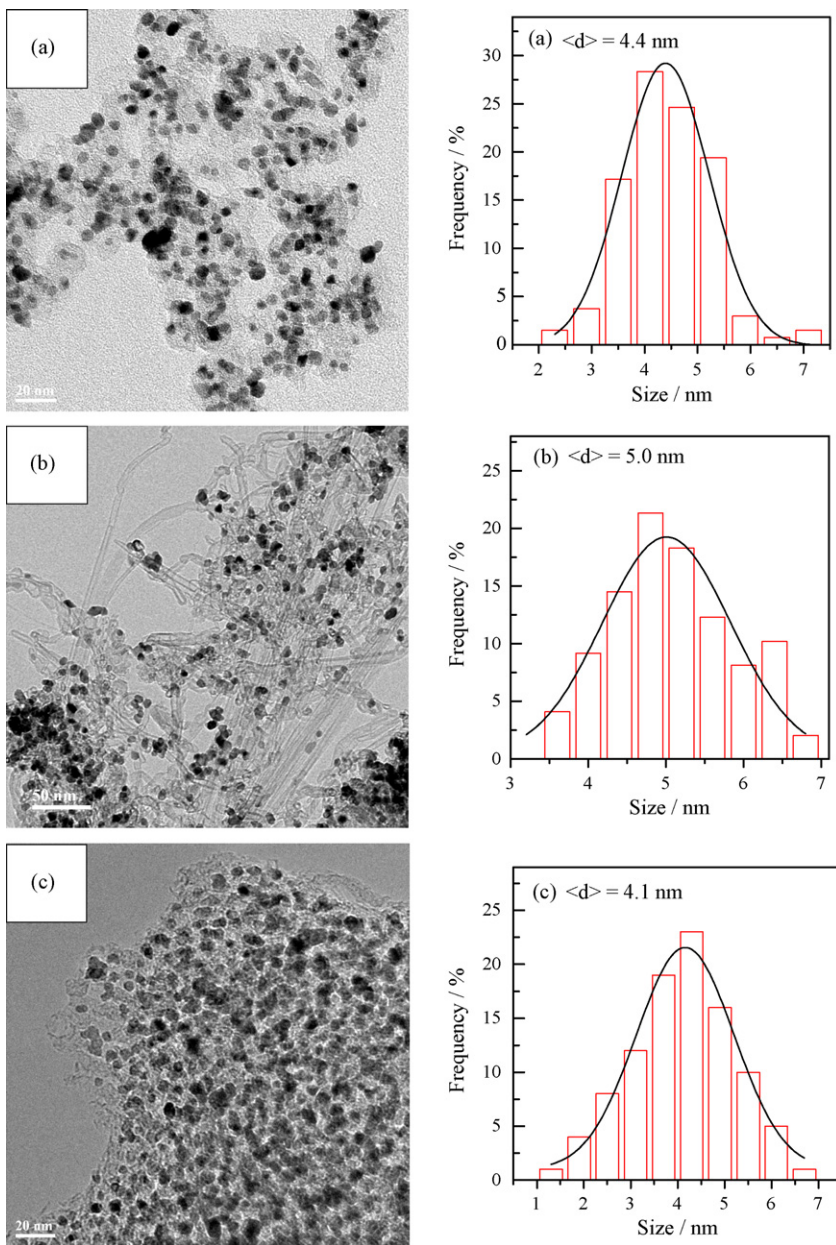


Fig. 2. TEM images and particle size distributions of (a) Pd₃Pt₁/XC-72R, (b) Pd₃Pt₁/SWCNTs and (c) Pd₃Pt₁/OMC catalyst at a metal loading of 50 wt%.

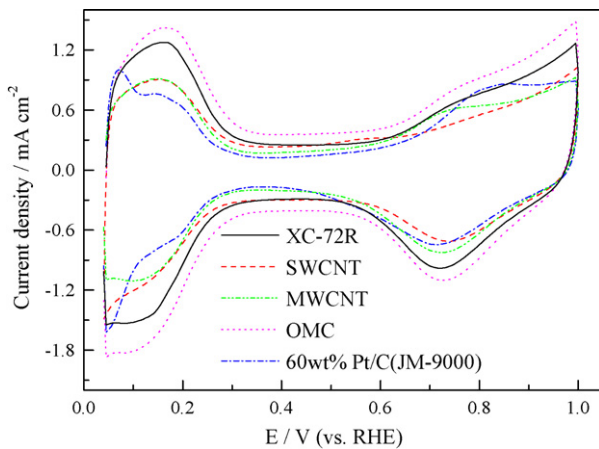


Fig. 3. Cyclic voltammograms (CVs) of different carbons supported Pd₃Pt₁ catalysts and commercial 60 wt% Pt/C(JM-9000) in 0.1 M HClO₄ at a scan rate of 50 mV s⁻¹.

alloy catalyst displays the highest ORR activity; its catalytic activity even outperforms that of the state-of-the-art Pt/C catalyst. From Fig. 4, the mass activity on the Pd₃Pt₁/OMC sample at 0.85 V is almost twice higher than that on Vulcan XC-72R supported catalyst. For the Pd₃Pt₁/OMC catalyst, the high surface area as well as the regular mesopores in OMC could be responsible for a better dispersion and a high utilization of the Pd₃Pt₁ nanoparticles [36], thus enhancing its ORR activity. On the other hand, the mesoporous structure enables the filling of the ionomer or polymer electrolyte to bring the catalyst particles close to the reactants, thus maximizing the triple-phase interface and facilitating the removal of water to avoid flooding [27].

For an efficient ORR catalyst, it is of importance to quantify the relative formation rates of water (four-electron pathway) or hydrogen peroxide (two-electron pathway) for the Pd₃Pt₁/OMC catalyst since the peroxide is corrosive toward the carbon materials and Nafion resins and is able to cause the oxidation destruction of the active sites and the defect sites in fuel cell catalysts and sup-

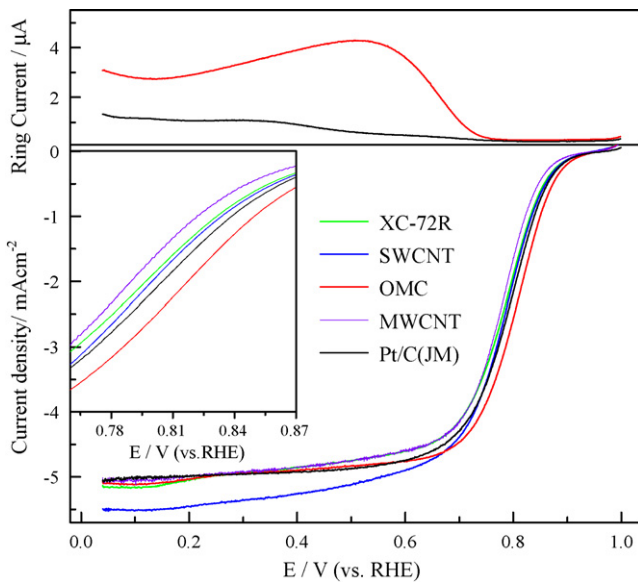


Fig. 4. Linear scan voltammograms (LSVs) of the different carbons supported Pd_3Pt_1 catalysts and commercial 60 wt% Pt/C(JM-9000) in 0.1 M HClO_4 saturated with pure O_2 (5 mV s^{-1} and 1600 rpm). The ring currents, RRDE data, for hydrogen peroxide production are contrasted.

ports [37]. RRDE data shown in Fig. 4 are illustrative of the ORR pathway on the Pt/C(JM-9000) and Pd_3Pt_1 /OMC catalyst. The ring current is found to be negligible compared to the disk current for potentials above 0.80 V, indicating that the ORR proceeds nearly without peroxide production. The ring current increases, starting from potentials lower than 0.75 V, and the amount of peroxide formed on the Pd_3Pt_1 /OMC alloy catalyst is slightly higher than that formed on pure Pt. The fraction of peroxide, $X_{\text{H}_2\text{O}_2}$, at a typical fuel cell operating potential of 0.70 V, was evaluated from disk current (I_D), ring current (I_R) and collection factor ($N = 0.20$) using the equation: $X_{\text{H}_2\text{O}_2} = 2I_R/N / (I_D + I_R/N)$. The fractions are 1.1 and 2.3% for the Pt/C and Pd_3Pt_1 /OMC catalysts, respectively. Thereby, the RRDE study during the ORR reveals negligible peroxide production on the Pd_3Pt_1 /OMC alloy catalyst, while the ORR on the Pd_3Pt_1 /OMC alloy catalyst undergoes a four-electron process leading to water formation.

Furthermore, Fig. 5a shows LSVs of the Pd_3Pt_1 /OMC catalyst in 0.1 M HClO_4 solution saturated with pure oxygen at different rotating rates. It can be seen that the ORR activity in the kinetic region is essentially the same at the different rotating rates. In the mixed and diffusion-controlled regions, the catalytic current increases with rotating speed. The plot of I^{-1} as a function of $\omega^{-1/2}$ is presented in Fig. 5b, where I denotes the current density, and ω angular frequency of rotation. All plots in Fig. 5b are nearly straight lines within the fitting error, indicating a first-order oxygen reduction reaction. From the Koutecky–Levich equation

$$\frac{1}{I} = \frac{1}{I_k} + \frac{1}{B\omega^{1/2}} \quad (1)$$

$$B = 0.62nFAD_{\text{O}_2}^{2/3}v^{1/6}C_{\text{O}_2} \quad (2)$$

where I is measured current density, I_k is the kinetic current density, and ω is the rotation rate. The published values [32,38] of diffusion coefficient of O_2 ($D_{\text{O}_2} = 1.93 \times 10^{-5} \text{ cm}^2 \text{ s}^{-1}$), the kinetic viscosity of the solution ($v = 8.93 \times 10^{-3} \text{ cm}^2 \text{ s}^{-1}$), and the concentration of dissolved O_2 in HClO_4 solution ($C_{\text{O}_2} = 1.18 \times 10^{-6} \text{ mol cm}^{-3}$) were used to calculate the number of electrons (n), where F is the Faraday constant and A is the electrode's geometric area (0.0707 cm^2). The constant B value was obtained from the slopes of the Koutecky–Levich plots. Subsequently, calculated results reveal

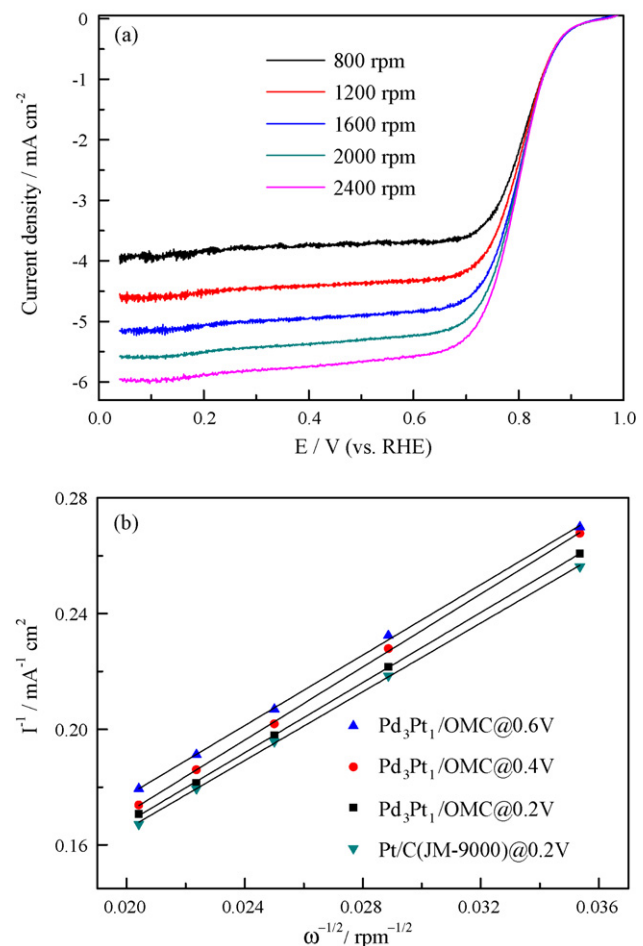


Fig. 5. (a) LSVs of the Pd_3Pt_1 /OMC catalyst in 0.1 M HClO_4 saturated with pure oxygen at a scan rate of 5 mV s^{-1} and at different rotation speeds. Current density is normalized to the geometrical surface area of the electrode. (b) Koutecky–Levich plots for the ORR in 0.1 M HClO_4 on the Pt/C(JM-9000) and Pd_3Pt_1 /OMC catalysts.

that the ORR on the Pt/C(JM-9000) and Pd_3Pt_1 /OMC catalyst predominantly follows a 4e^- pathway, in good agreement with RRDE results.

It is well known that the crossover of methanol from the anode to the Pt cathode can lead to a further reduction in cell voltage, by ca. 200–300 mV. There is a competitive reaction between oxygen reduction and methanol oxidation on Pt-based cathodes. Thus, it is highly desirable to develop selective-ORR electrocatalysts that have a high methanol tolerance for DMFC applications. Fig. 6 reveals the ORR performances on the Pt/C and Pd_3Pt_1 /OMC catalysts in the presence of 0.5 M CH_3OH solution at a scan rate of 5 mV s^{-1} and rotating speed of 1600 rpm. The current density of the methanol oxidation reaction on the Pd_3Pt_1 /OMC catalysts is much lower than that on the Pt/C catalyst, indicating that the alloy catalysts for methanol oxidation are less active than the Pt/C catalyst. This observation is consistent with the fact that Pd is inactive for methanol oxidation in acidic solution and the dissociative chemisorption of methanol requires the existence of at least three adjacent Pt ensembles [39], which is influenced by the presence of Pd atoms around the Pt active sites that are expected to block methanol adsorption on Pt sites due to the dilution effect.

3.3. MEA test

To explore the possible application of the Pd_3Pt_1 /OMC in a DMFC, a performance comparison of two passive DMFCs with

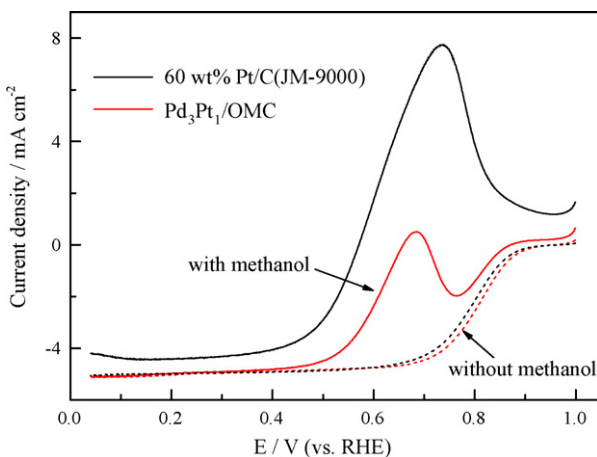


Fig. 6. LSVs of the Pt/C(JM-9000) and $\text{Pd}_3\text{Pt}_1/\text{OMC}$ catalysts in $0.1 \text{ M HClO}_4 + 0.5 \text{ M CH}_3\text{OH}$ solution saturated with pure O_2 at 5 mV s^{-1} and 1600 rpm .

OMC-supported Pd–Pt alloy and commercial Pt/C(JM-9000) as the cathode catalysts is shown in Fig. 7. It can be seen that the open circuit voltage of the passive DMFC using $\text{Pd}_3\text{Pt}_1/\text{OMC}$ as cathode catalyst is slightly higher than that with Pt/C cathode. Less methanol crossover from the anode to the cathode at the beginning may be the reason to underestimate the methanol poisoning effect on the Pt catalyst. Importantly, the as-prepared $\text{Pd}_3\text{Pt}_1/\text{OMC}$ catalyst exhibited a better performance with low polarization losses at both low and high current densities than the Pt/C catalyst. When using 3 M methanol solution, the passive DMFC consisting of the $\text{Pd}_3\text{Pt}_1/\text{OMC}$ as the cathode catalyst delivers the enhanced peak power density of 25.3 mW cm^{-2} with respect to the peak power density of 21.8 mW cm^{-2} observed for the DMFC with Pt/C cathode, which is consistent with the LSV results that the $\text{Pd}_3\text{Pt}_1/\text{OMC}$ exhibits a better methanol-tolerant ORR activity than the Pt/C. To further identify the methanol tolerance of the $\text{Pd}_3\text{Pt}_1/\text{OMC}$, 5 M methanol solution was used for two passive DMFCs. The maximal power density of the passive DMFC using $\text{Pd}_3\text{Pt}_1/\text{OMC}$ cathode decreases to 23.8 mW cm^{-2} , due to an increased crossover at high methanol concentration. However, the maximal power density of the passive DMFC using Pt/C catalyst decreases to ca. 17.1 mW cm^{-2} . These results again assess that the $\text{Pd}_3\text{Pt}_1/\text{OMC}$ exhibits a high methanol tolerance during the ORR.

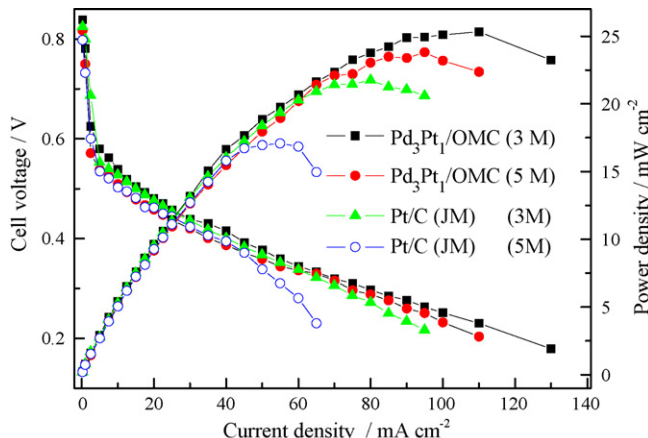


Fig. 7. Polarization curves of two passive DMFCs with the Pt/C(JM-9000) and $\text{Pd}_3\text{Pt}_1/\text{OMC}$ as cathode catalysts operated at 3 and 5 M methanol solution, respectively.

4. Conclusions

A variety of carbon materials were used to support the Pd–Pt alloy nanoparticles with a Pd/Pt atomic ratio of 3:1, whose structures and catalytic activities were characterized by XRD, TEM and RDE/RRDE techniques. It is remarkable that the OMC-supported Pd_3Pt_1 catalyst exhibits the highest mass activity for the ORR among the investigated carbon supports. The high ORR activity as well as good tolerance to methanol on the $\text{Pd}_3\text{Pt}_1/\text{OMC}$ alloy catalyst suggests that the $\text{Pd}_3\text{Pt}_1/\text{OMC}$ may be an economically viable candidate to replace Pt as a cathode catalyst in a DMFC.

Acknowledgements

The authors would like to thank the NSF of China (20673136 and 20706056), the National “863” High-Technology Research Programs of China (2007AA05Z107, 2006AA05Z136 and 2008AA05Z102), the 100 People Plan Program of the CAS and the Knowledge Innovation Engineering of the CAS for support of this work. W.H. also thanks the Graduate Student Innovation Foundation of Jiangsu Province (CX09B-076Z).

References

- J.L. Zhang, M.B. Vukmirovic, K. Sasaki, A.U. Nilekar, M. Mavrikakis, R.R. Adzic, *J. Am. Chem. Soc.* 127 (2005) 12480–12481.
- D.R. Rolison, P.L. Hagans, K.E. Swider, J.W. Long, *Langmuir* 15 (1999) 774–779.
- J.J. Wang, G.P. Yin, G.J. Wang, Z.B. Wang, Y.Z. Gao, *Electrochem. Commun.* 10 (2008) 831–834.
- A. Sarkar, A.V. Murugan, A. Manthiram, *J. Phys. Chem. C* 112 (2008) 12037–12043.
- W.E. Mustain, K. Kepler, J. Prakash, *Electrochem. Commun.* 8 (2006) 406–410.
- A. Sarkar, A.V. Murugan, A. Manthiram, *J. Mater. Chem.* 19 (2009) 159–165.
- W.M. Wang, Q.H. Huang, J.Y. Liu, Z.Q. Zou, M.Y. Zhao, W. Vogel, H. Yang, *J. Catal.* 266 (2009) 156–163.
- W. He, J.Y. Liu, Y.J. Qiao, Z.Q. Zou, X.G. Zhang, D.L. Akins, H. Yang, *J. Power Sources* 195 (2010) 1046–1050.
- H. Liu, W. Li, A. Manthiram, *Appl. Catal. B: Environ.* 90 (2009) 184–194.
- Y.H. Cho, B. Choi, Y.H. Cho, H.S. Park, Y.E. Sung, *Electrochem. Commun.* 9 (2007) 378–381.
- H.Q. Li, G.Q. Sun, N. Li, S.G. Sun, D.S. Su, Q. Xin, *J. Phys. Chem. C* 111 (2007) 5605–5617.
- J.B. Joo, Y.J. Kim, W. Kim, N.D. Kim, P. Kim, Y. Kim, J. Yi, *Korean J. Chem. Eng.* 25 (2008) 770–774.
- D. Mirabile Gattia, M.V. Antisari, L. Giorgi, R. Marazzi, E. Piscoppiello, A. Montone, S. Bellitto, S. Licoccia, E. Traversa, *J. Power Sources* 194 (2009) 243–251.
- E. Antolini, *Appl. Catal. B: Environ.* 88 (2009) 1–24.
- W.Z. Li, C.H. Liang, W.J. Zhou, J.S. Qiu, Z.H. Zhou, G.Q. Sun, Q. Xin, *J. Phys. Chem. B* 107 (2003) 6292–6299.
- Z.Q. Liu, J. Ma, Y.H. Cui, B.P. Zhang, *Appl. Catal. B: Environ.* 92 (2009) 301–306.
- F. Alcaide, G. Alvarez, O. Miguel, M. Jesus Lazaro, R. Moliner, A. Lopez-Cudero, J. Solla-Gullon, E. Herrero, A. Aldaz, *Electrochim. Commun.* 11 (2009) 1081–1084.
- R. Ryoo, S.H. Joo, M. Kruk, M. Jaroniec, *Adv. Mater.* 13 (2001) 677–681.
- J. Ding, K. Chan, J. Ren, F. Xiao, *Electrochim. Acta* 50 (2005) 3131–3141.
- A. Hayashi, H. Notsu, K. Kimijima, J. Miyamoto, I. Yagi, *Electrochim. Acta* 53 (2008) 6117–6125.
- S.H. Joo, K. Kwon, D.J. You, C. Pak, H. Chang, J.M. Kim, *Electrochim. Acta* 54 (2009) 5746–5753.
- S.H. Joo, S.J. Choi, I. Oh, J. Kwak, Z. Liu, O. Terasaki, R. Ryoo, *Nature* 412 (2001) 169–172.
- S. Vengatesan, H.J. Kim, S.K. Kim, I.H. Oh, S.Y. Lee, E. Cho, H.Y. Ha, T.H. Lim, *Electrochim. Acta* 54 (2008) 856–861.
- G. Wu, D.Y. Li, C.S. Dai, D.L. Wang, N. Li, *Langmuir* 24 (2008) 3566–3575.
- W.M. Wang, Q.H. Huang, J.Y. Liu, Z.Q. Zou, Z.L. Li, H. Yang, *Electrochim. Commun.* 10 (2008) 1396–1399.
- S.H. Joo, C. Pak, D.J. You, S. Lee, H.I. Lee, J.M. Kim, H. Chang, D. Seung, *Electrochim. Acta* 52 (2006) 1618–1626.
- H. Chang, S.H. Joo, C. Pak, J. Mater. Chem. 17 (2007) 3078–3088.
- H. Meng, S. Sun, J. Masse, J. Dodelet, *Chem. Mater.* 20 (2008) 6998–7002.
- T. Yuan, Z.Q. Zou, M. Chen, Z.L. Li, B.J. Xia, H. Yang, *J. Power Sources* 192 (2009) 423–428.
- A.E. Cordero-Borboa, E. Sterling-Black, A. Gomez-Cortes, A. Vazquez-Zavala, *Appl. Surf. Sci.* 220 (2003) 169–174.
- K.D. Beard, J.W. Van Zee, J.R. Monnier, *Appl. Catal. B: Environ.* 88 (2009) 185–193.
- J.H. Yang, J.Y. Lee, Q.B. Zhang, W.J. Zhou, Z.L. Liu, *J. Electrochim. Soc.* 155 (2008) B776–B781.
- G. Wu, B.Q. Xu, *J. Power Sources* 174 (2007) 148–158.

- [34] A. Kongkanand, K. Vinodgopal, S. Kuwabata, P.V. Kamat, *J. Phys. Chem. B* 110 (2006) 16185–16188.
- [35] Y.H. Shih, G.V. Sagar, S.D. Lin, *J. Phys. Chem. C* 112 (2008) 123–130.
- [36] V. Raghubeer, A. Manthiram, *J. Electrochem. Soc.* 152 (2005) A1504–A1510.
- [37] X.G. Li, S. Park, B.N. Popov, *J. Power Sources* 195 (2010) 445–452.
- [38] W.M. Wang, D. Zheng, C. Du, Z.Q. Zou, X.G. Zhang, B.J. Xia, H. Yang, D.L. Akins, *J. Power Sources* 167 (2007) 243–249.
- [39] J. Salgado, E. Antolini, E.R. Gonzalez, *Appl. Catal. B: Environ.* 57 (2005) 283–290.